

Supplementary Information

Partial Cation Substitution Reduces Iodide Ion Transport in Lead Iodide Perovskite Solar Cells

Dominic W. Ferdani¹, Samuel R. Pering¹, Dibyajyoti Ghosh^{1,2}, Peter Kubiak¹, Alison B. Walker², Simon E. Lewis¹, Andrew L. Johnson¹, Peter J. Baker³, M. Saiful Islam^{1*}, Petra J. Cameron^{1*}

¹*Department of Chemistry, University of Bath, Bath BA2 7AY, UK*

²*Department of Physics, University of Bath, Bath BA2 7AY, UK*

³*ISIS Neutron & Muon Source, STFC Rutherford Appleton Laboratory, Didcot OX11 0QX, UK*

Contents

(A) Methods	Page 2
(B) Optical and NMR analysis	Page 5
(C) Computational information	Page 7
(D) Impedance Spectroscopy.....	Page
13	
(E) μSR Information.....	Page
20	

(A) Methods

(i) Synthesis, XRD and microscopy. Reagents were purchased from the following suppliers and used without further purification unless stated otherwise: PbI_2 (99%), *N,N*-Dimethylformamide (DMF) (99.8 %) and d_3 -methylamine (99 %) from Sigma Aldrich and methyl ammonium iodide (99 %) from Greatcell Solar. All fabrication was carried out in a Plas-Labs dry box, which controls the humidity at approximately 8 %. All NMR spectra were acquired using a Bruker 500 MHz instrument at 298 K unless otherwise stated. X-ray diffraction patterns were obtained using a Bruker axs D8 advance powder X-ray diffractometer with $\text{Cu K}\alpha$ source and Ge monochromator.

AzI was synthesised based on a previously reported procedure.¹ All other cations were obtained from Greatcell Solar, except CsI (Alfa). $\text{CD}_3\text{NH}_3\text{PbI}_3$ was synthesised as follows: CD_3NH_2 (10g) was slowly bubbled into ethanol (200mL) under an inert atmosphere at -94°C . 58 wt% hydroiodic acid (1eq) was added to this solution and the reaction allowed to heat to room temperature and left stirring for 16 hours. The ethanol was removed *in vacuo* and the resulting brown solid was washed with diethyl ether three times before recrystallising with ethanol and diethyl ether leading to the formation of a white solid which was confirmed to be $\text{CD}_3\text{NH}_3\text{I}$ iodide by NMR. Yield (40.95 g 86%). To convert to $\text{CD}_3\text{ND}_3\text{I}$, $\text{CD}_3\text{NH}_3\text{I}$ (20 g) was dissolved in D_2O (25 eq, 55 mL) and stirred at room temperature for 16 hours. The solvent was removed *in vacuo* and the procedure repeated twice to maximise proton exchange. The resulting product was, again, confirmed using ^2H and ^{13}C NMR.

The perovskite powders were synthesised by hot-casting. To prepare d_6 - MAPbI_3 powders, a 1.9 M PbI_2 and $\text{CH}_3\text{NH}_3\text{I}$ DMF solution was prepared and stirred at 60°C for an hour before it was cast onto a clean glass petri dish at 110°C and then left for an hour to form a black film. The film was scratched from the petri dish to produce MAPbI_3 powder as confirmed by XRD. The deuterium content of the d_6 - MAPbI_3 powder was confirmed to be 83% by integrating ^2H NMR. For the substituted perovskites 5 mol% of the MA was replaced with the appropriate

cation and the same synthesis procedure was followed. The stoichiometry of the final materials was determined using ^1H NMR.

Atomic Force Microscopy (AFM) imaging was performed using a Nanosurf Easyscan 2 FlexAFM system in phase contrast mode using a Tap-190-Al-G tip.

(ii) Solar cell fabrication and analysis. Tec 15 FTO substrates were prepared by etching with HCl and Zn powder to the desired pattern. They were then cleaned thoroughly by sonicating at 80 °C in Helmanex 2wt% in water followed by water, acetone, propan-2-ol and ethanol before finally being cleaned with UV/Ozone for 20 minutes. A NiO_x HTM layer was prepared by spin-coating a 50 mgmL^{-1} solution of nickel (II) acetate (Sigma) in 2-methoxyethanol (Sigma). The resulting films were annealed in air at 500 °C for 30 minutes.

Perovskite, PCBM and bathocuproine film deposition was performed in an N_2 -filled dry box. A 1.25:1.25 molar solution of MAI and PbI_2 in 4:1 DMF: DMSO was spin-coated at 4000 rpm for 30 seconds. An anti-solvent treatment was carried out with 200 μL ethyl acetate. For mixed cation perovskites, MAI was replaced with the appropriate cation so that the molar ratio was 95:5 MAI:xI. Films were annealed for 15 minutes at 100 °C. 20 mgmL^{-1} PCBM (Ossila) in chlorobenzene was spin-coated onto the perovskite film at 3000 rpm for 30 seconds, followed by a 0.5 mgmL^{-1} solution of bathocuproine (Sigma) in ethanol for 6000 rpm for 30 seconds. A silver contact was evaporated from silver wire (Alfa Aesar) at 10^{-6} bar.

Current density-voltage curves were measured using a 2400 series Sourcemeeter (Keithley Instruments), under simulated AM1.5 sunlight at 100 mW cm^{-2} irradiance generated using a class AAA solar simulator (TS-Space Systems) at room temperature in air. The intensity was calibrated using a certified silicon reference cell (Fraunhofer). The active area of the pixels was 0.0625 cm^2 , measured using a mask of the same area. Voltage scans were taken from 1.1 V (preconditioning time 5s) to 0 V at 100 mVs^{-1} . EIS measurements were taken on a Solartron modulab, measurements were taken under 73 mW cm^{-2} illumination at open circuit between 1MHz and 5MHz with a 10 mV perturbation.

(iii) Muon spin relaxation. μSR studies were performed at the ISIS pulsed muon facility using the EMU instrument. Approximately 1 gram of sample was packed into a 4 cm^2 packet made from silver foil which was subsequently attached to the sample stage. The temperature was controlled between 40 K and 410 K using a closed cycle refrigerator and a hot stage. Measurements at four different longitudinal fields (0, 5, 10 and 20 G) were taken for each temperature. To initially calibrate the instrument a transverse field of 100 G was applied.

(iv) *Ab initio* simulations. The computational methodology for modelling ion transport in the solid-state is well developed and has been extensively validated for perovskites. The perovskite structures and energies were calculated using density functional theory (DFT) methods (employing the *ab initio* code CP2K)² with further details given in Section C below. A 3×2×2 supercell (576 atoms) of the tetragonal unit cell was modelled. We employed the mixed Gaussian and plane-wave method, GGA of the PBEsol form, analytical dual-space pseudopotentials and Grimme-type (DFT-D3) dispersion corrections. Activation energies for diffusion processes were computed from the total energy difference between the diffusing species in their ground-state configuration and at the saddle point of the diffusion process. Ion transport mediated by ion vacancies was examined using nudged elastic band (NEB) and constrained energy minimisation methods.

(B) Optical and NMR analysis

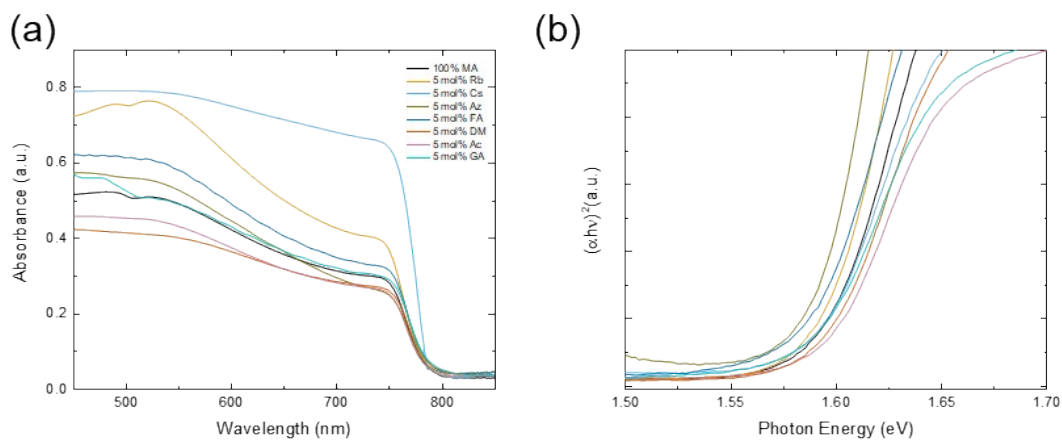


Figure S1. Optical analysis of the 8 mixed cation perovskite films (a) absorbance plot (b) Tauc plot.

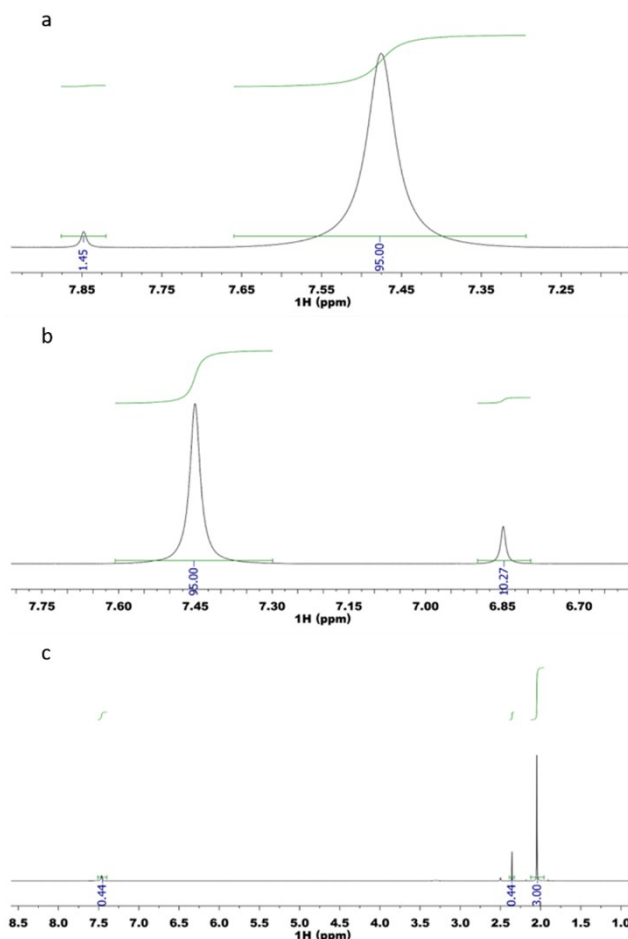


Figure S2. ^1H NMR spectra a) $\text{MA}_{0.95}\text{FA}_{0.05}\text{PbI}_3$, b) $\text{MA}_{0.95}\text{GA}_{0.05}\text{PbI}_3$ and c) $\text{MA}_{0.95}\text{Cs}_{0.05}\text{PbI}_3$ in d_6 -DMSO.

For Fig. S2 the stoichiometry can be calculated from the integral comparison. In the case of Fig. S2c, the Cs⁺ cation does not have any hydrogens to compare therefore known molarities of both the perovskite and acetonitrile were mixed in the NMR sample. The addition of the acetonitrile (peak at 2.1 ppm) gives a reference number of hydrogens that the perovskite peaks can be compared with and from that the number of moles of MA⁺ can be calculated. Once the amount of MA⁺ is calculated any unaccounted-for moles can then be attributed to Cs⁺ substitution.

Table S1. Ionic volumes for different A-site cations and band gap of MA_{0.96}A_{0.04}PbI₃ from *ab initio* calculations.

A-site Cation	Ionic Volume (Å³)	Bandgap (eV)
Rubidium	10.17	1.35
Caesium	48.13	1.35
Methylammonium	53.45	1.35
Azetidinium	103.04	1.35
Formamidinium	62.29	1.35
Dimethylammonium	71.17	1.36
Acetamidinium	96.95	1.36
Guanidinium	72.90	1.36

(C) Computational information

(i) Methods & stability calculations. The ground state structures and energies of $\text{CH}_3\text{NH}_3\text{PbI}_3$ and mixed cation perovskite were calculated using density functional theory methods as implemented in the CP2K code.² Here we employed the mixed Gaussian and plane-wave method (QUICKSTEP formalism),³ GGA of the PBEsol form,⁴ analytical dual-space pseudopotentials⁵ and Grimme type dispersion corrections.⁶ A $3 \times 2 \times 2$ supercell (48 A-cations; 576 atoms) of the tetragonal unit cell was considered to model the parent MAPbI_3 . Such a large supercell enabled us to model the mixed cation perovskite cells. For each composition, several ordered configurations of the A-site species were examined, and the lowest energy structure was considered for further study.

As indicated by experimental observations, we considered the following formation pathway for these mixed A-cation perovskites using Cs as an example:



The corresponding formation enthalpy can be formulated as,

$$\Delta H = E[\text{MA}_{1-x}\text{Cs}_x\text{PbI}_3] - (1-x) E[\text{MAI}] - x E[\text{CsI}] - E[\text{PbI}_2]$$

where $E[\text{MA}_{1-x}\text{Cs}_x\text{PbI}_3]$, $E[\text{MAI}]$, $E[\text{CsI}]$ and $E[\text{PbI}_2]$ are the total energies per formula unit.

As the equation suggests, a negative enthalpy value indicates that the reaction is exothermic and thus the perovskite phase is thermodynamically stable against the reactants. As recent studies have shown that the vibrational and cationic rotational entropy does not affect the relative phase stability of the hybrid perovskites significantly.^{7,8}

Activation energies for defect mediated ion diffusion processes have been computed from the total energy difference between the diffusing species in their ground-state configuration and at the saddle point during the diffusion process. The climbing-image nudged elastic band (CI-NEB) method has been used to calculate the lowest energy migration path. The convergence criteria of the total energy was set to 1×10^{-6} eV. A maximum force of 0.02 eV/Å has been considered to converge the minimum energy path in the CI-NEB calculations. We perform linear interpolation between the end-points to prepare initial MEPs using 16 intermediate images. Note that test calculations increasing the number of images to 24 does not

affect the migration activation energy. The use of a large simulation cell ensures an inter-image distance of at least ~ 17 Å, avoiding spurious interactions between defects.

The molecular volume of A-site cations is defined as the volume inside a contour of 0.001 electrons/Bohr³ electron density. We used *Gaussian16* program package to compute the molecular volumes.⁹

(ii) Structure and energetics. At room temperature, MAPbI₃ has a tetragonal phase with space group *I4/mcm*.¹⁰ As shown in Fig. S3, the PbI₆ octahedra are corner-connected and has typical ‘out-of-phase’ rotation along the c-axis that is a⁰a⁰c⁻ tilting according to Glazer notation. In the tetragonal phase, the PbI₆ octahedra comprise of two non-equivalent halogen sites, (c) axial (I_{axial}) and (d) equatorial (I_{equatorial}) (see Fig. S3c,d). Iodide migration can occur between two adjacent equatorial sites, or between an equatorial and an axial site.

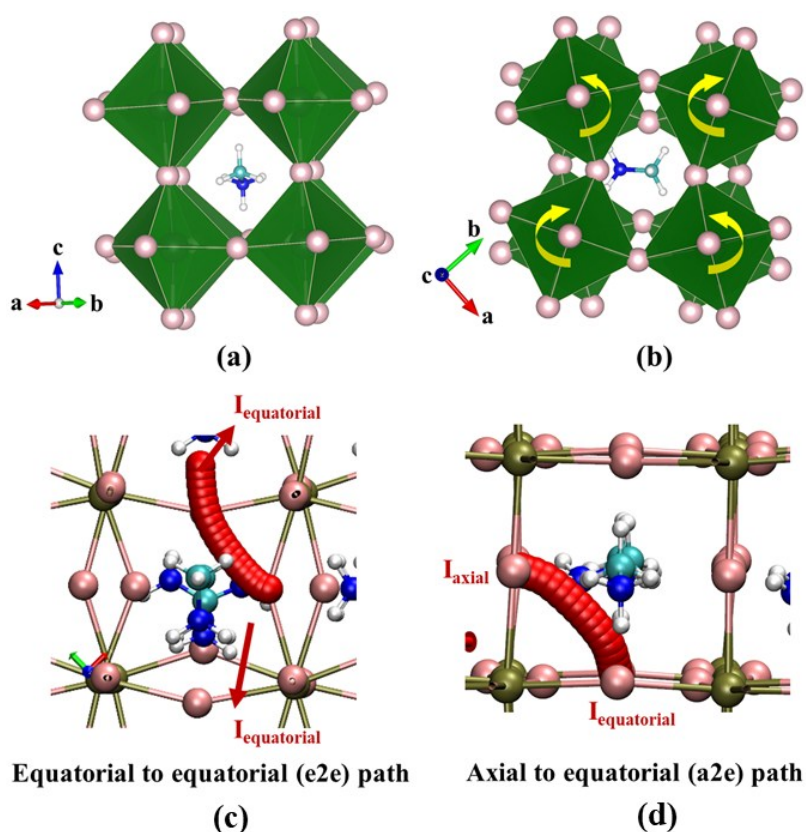


Figure S3. Schematic structure of the tetragonal phase of MAPbI₃ (a) parallel and (b) perpendicular to *ab*-plane. Yellow arrows in (b) indicate the direction of the rigid rotation of octahedra. (c, d) The migration paths for iodide vacancies in tetragonal MAPbI₃. Key: hydrogen (white), carbon (cyan), nitrogen (blue), iodine (pink), lead (brown).

The fully relaxed lattice parameters of MAPbI₃ are in very good agreement with the experimental values where the difference is within 3%.¹⁰ To determine the structural effect of cation substitution on the MAPbI₃ structure, we first look into the total volume of the lattice. As shown in Fig. S4, the volume per formula unit changes according to the size of the substituent cation. Starting with the parent MAPbI₃ structure, it is clear that the lattice volume expands with the substitution of MA for larger cations (FA, Az, DM, Ac and GA) or contracts with the substitution of smaller Cs cations. The change in the lattice volume with only a 5mol% substitution of cation indicates the mechanical softness of the halide perovskites. The small shifts in the XRD peaks for the perovskite phase also support the volume change upon cation substitution (Fig. S4b).

We further examine the local structural distortion upon cation substitution. The MA_{0.96}GA_{0.04}PbI₃ has been examined closely as a representative system. As shown in Fig. S4c, the Pb/I bonds near to the GA cations distort. The larger cationic volume of GA than MA exerts chemical pressure on the neighbour inorganic lattice, expanding and distorting it locally. Note that cations smaller than MA also exhibits similar kind of lattice distortion by contracting the whole lattice.

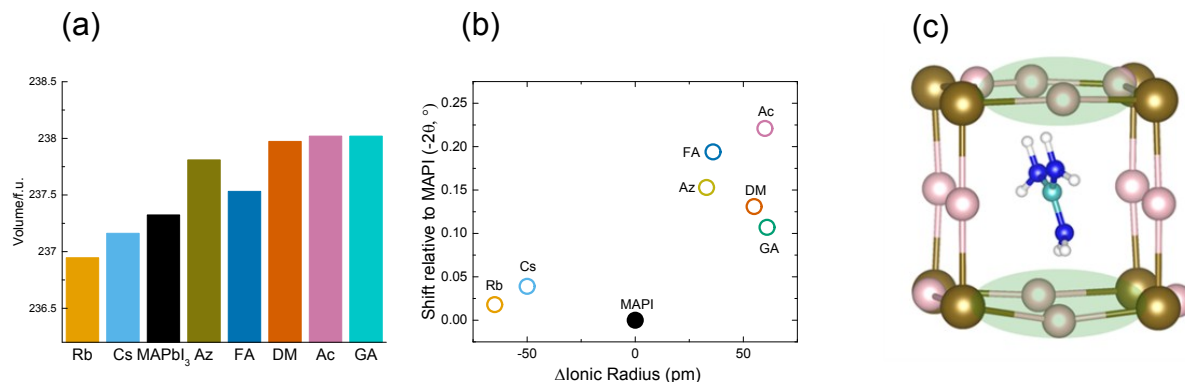


Figure S4. Structural properties of the MA_{0.96}A_{0.04}PbI₃ perovskites. (a) Optimized volume per formula unit of each substituted perovskite. (b) Shift in the MAPbI₃ (220) peak with the incorporation of 5 mol% of cations. (c) Computationally optimized MA_{0.96}GA_{0.04}PbI₃ lattice with the distorted Pb-I bonds shown in the shaded green area. GA incorporation leads to the repulsion of the surrounding iodide ions due to steric factors.

(iii) Electronic properties. By examining the electronic properties, we find an insignificant effect of cation substitution on the band gap of these hybrid perovskites (Table S1) which is in line with the experimental UV-Vis measurements. We note that due to the use of semi-local PBEsol exchange functionals the band gaps of these perovskites have been underestimated systematically. As shown in Fig. S5, the valence band formed by the antibonding between 5p

of I and 6s of Pb whereas the nonbonding 6p-orbitals of Pb contribute dominantly to the conduction band. Thus, the band edges of these lead halide perovskites largely depend on the chemical nature and structure of the inorganic frame. As the A-cations do not contribute directly to the band edges, substitution of these cations does not have any major effect on the electronic nature of the valence and conduction bands. It has been demonstrated that the A-cation can indirectly affect the band edges by distorting the inorganic frame of the entire halide perovskite system. However, in our case, as the structural distortion due to cation substitution is very local in nature, we do not find any significant change in the nature of the band edges or values of the band gap.

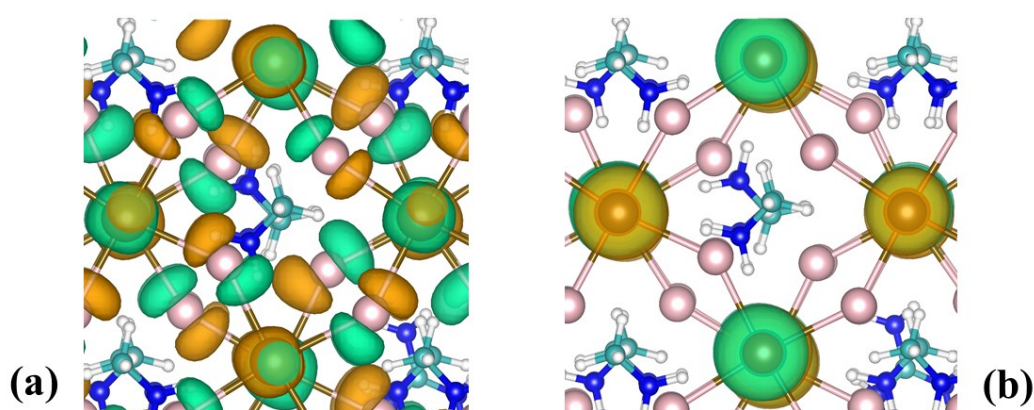


Figure S5. Charge density plots (a) valence band and (b) conduction band in $\text{MA}_{0.96}\text{GA}_{0.04}\text{PbI}_3$.

To understand the charge distribution in the hybrid perovskites, we further plot the two- and three-dimensional electrostatic potential map (ESP) in Fig. S6a-e. The ESP plots for the MAPbI_3 reveal that iodide ions are the most electronegative sites in the lattice (Fig. S6a-c). Furthermore, the nitrogen atoms of MA cations are also electronegative in nature, but are potentially weaker sites than the iodide. Plotting the ESP for $\text{MA}_{0.96}\text{GA}_{0.04}\text{PbI}_3$, we find that the cation mixing distorts the local Pb/I lattice to a small extent and keeps the overall electrostatic environment almost unaltered with respect to the parent perovskite (Fig. S6d,e).

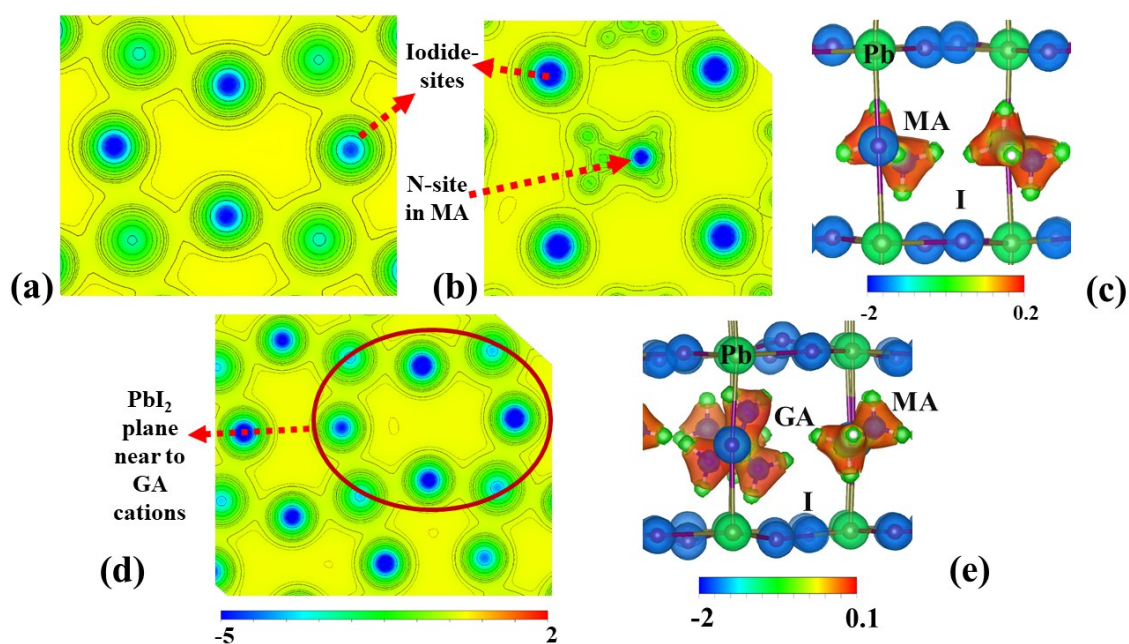


Figure S6. Electrostatic Potential Maps for MAPbI_3 and mixed cation perovskites. Two-dimensional electrostatic potential contour maps for (a) PbI_2 plane and (b) MAI plane of MAPbI_3 and (c) three-dimensional ESP plot for the whole lattice. For $\text{MA}_{0.96}\text{GA}_{0.04}\text{PbI}_3$, (d) two-dimensional and (e) three-dimensional ESP plot of lattice near to the GA cation. The colour scale has been shown for each map.

To find out the effect of iodide vacancies on the ESP of the crystal, we have calculated the potential map of the MAPbI_3 lattice with an MAI defect in Fig. S7a,b. The ESP plot in Fig. S7a,b shows the missing iodide site. However, we do not find any charge accumulation near to the iodide defect site.

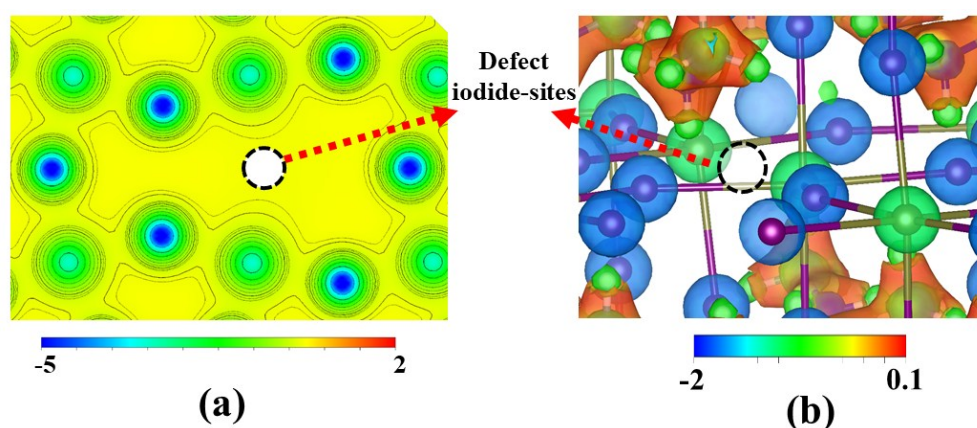


Figure S7. Electrostatic Potential Maps for MAPbI_3 with defects. (a) Two-dimensional electrostatic potential contour maps for a PbI_2 plane with iodide vacancy in MAPbI_3 and (b) corresponding three-dimensional ESP plot. The colour scale has been shown for each map.

(iv) Ion migration. Our calculations demonstrate that the iodide vacancy in the equatorial (e) position is energetically more stable than the axial (a) one. As reported in Table S2, we have calculated the activation barrier for both the inequivalent ion migration path for MA_I .

$x\text{GA}_x\text{PbI}_3$ ($x = 0, 0.04, 0.25$) and $\text{MA}_{0.75}\text{Cs}_{0.25}\text{PbI}_3$. Regardless of the A-cation composition, the hopping between an equatorial and an axial site always exhibits a higher energy barrier for migration than hopping between two equatorial sites. In a polycrystalline sample where the orientation of individual grains is random, the higher migration barrier should be considered as the representative one for long-range ion-diffusion. The energy profile along the iodide migration path is shown in Fig. S8. We also calculate the migration barrier for MA and GA cations in the parent and the mixed cation perovskites (Table S2). In line with previous studies, we find much higher activation energies for A-cation migration than for iodide migration, confirming that significant A-cation migration is unlikely.

Table S2. Activation Energies (E_A) of iodide and A-cation migration in MAPbI_3 and $\text{MA}_{1-x}\text{GA}_x\text{PbI}_3$ ($x = 0.04, 0.25$) perovskites.

Perovskite	E_A for I (e to a) (eV)	E_A for I (e to e) (eV)	E_A for MA (eV)	E_A for GA (eV)
MAPbI_3	0.44	0.42	0.67	-
$\text{MA}_{0.96}\text{GA}_{0.04}\text{PbI}_3$	0.48	0.44	0.71	1.09
$\text{MA}_{0.75}\text{GA}_{0.25}\text{PbI}_3$	0.78	0.73	-	-
$\text{MA}_{0.75}\text{Cs}_{0.25}\text{PbI}_3$	0.50	0.44	-	-

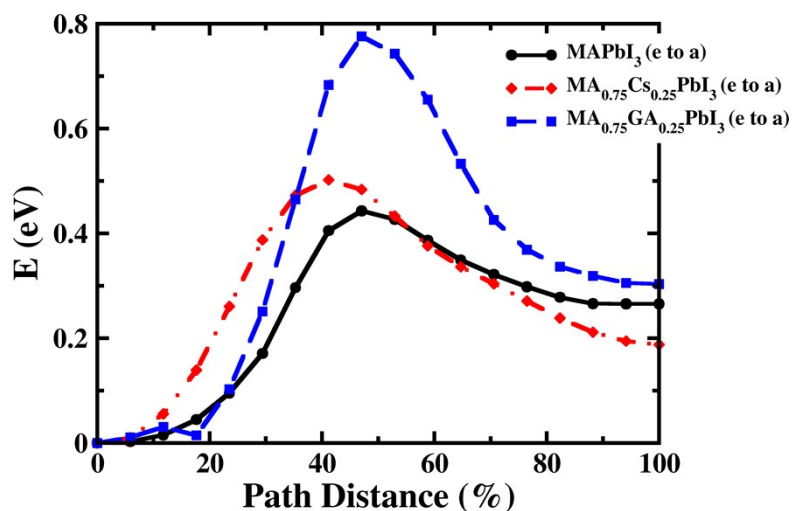


Figure S8. Energy profile along the migration paths. Computed migration energies for iodide migration in MAPbI_3 , $\text{MA}_{0.75}\text{Cs}_{0.25}\text{PbI}_3$ and $\text{MA}_{0.75}\text{GA}_{0.25}\text{PbI}_3$.

To find out the effect of substituted organic A-cation orientation on the calculated activation energies for the iodine migration, we have considered several different conformations of GA in $\text{MA}_{0.75}\text{GA}_{0.25}\text{PbI}_3$ (see Fig. S9 a-c). For instance, we find no significant change in the activation energy for iodide migration with different GA conformations. The

calculations exhibit the activation energy values from the range 0.71-0.78 eV for several different conformations with highest barrier value as 0.78 eV, reported in the study. Thus, for iodide migration, there is no major dependence on the conformations of the GA cation. Calculating the migration barrier for iodide hopping far from the substituted A-cation cage, we find similar activation energies compared to the parent MAPbI₃ lattice. Nevertheless, considering the long-range iodide ion diffusion from one electrode to another in halide perovskite-based solar cells, the migrating iodide ions will encounter cages with substituted A-cations along their diffusion paths. Hence, long-range iodide diffusion through the perovskite lattice will need to traverse the rate-limiting barrier of 0.78 eV.

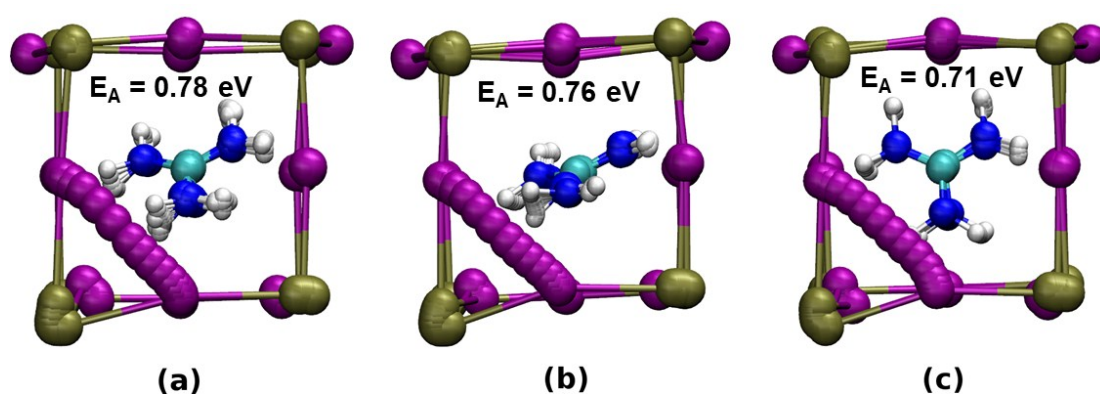


Figure S9. Iodide migration and effect of cation orientation. *Ab initio* simulations of ion transport paths in MA_{0.75}GA_{0.25}PbI₃ with different (a-c) GA conformations. The migration path and barrier energy depend do not depend significantly on the GA cation orientation in the cage. (For clarity, we have shown only the cage directly involved in the iodide hopping process.)

(D) Impedance spectroscopy

Table S3. Average PSC parameters for MA_{0.95}A_{0.05}PbI₃ (with standard deviation over at least 17 pixels)

A cation	V _{OC} (V)	J _{SC} (mAcm ⁻²)	FF (%)	η (%)
Rb	0.99 (±0.01)	15.3 (±1.6)	61.4 (±4.0)	9.3 (±1.2)
Cs	0.98 (±0.033)	17.42 (±1.36)	58.67 (±5.74)	10.07 (±1.38)
MA	1.00 (±0.016)	16.18 (±1.86)	60.37 (±5.31)	9.78 (±1.77)
Az	0.98 (±0.012)	13.42 (±2.02)	63.95 (±4.88)	8.43 (±2.39)
FA	0.96 (±0.021)	15.31(±1.82)	65.3 (±5.51)	9.57 (±1.81)
DM	0.97 (±0.02)	14.97 (±2.36)	61.17 (±4.83)	8.96 (±1.93)
Ac	0.96 (±0.031)	15.62 (±1.80)	63.34 (±7.92)	9.52 (±1.70)
GA	0.98 (±0.016)	16.39 (±1.60)	56.68 (±5.77)	9.06 (±0.79)

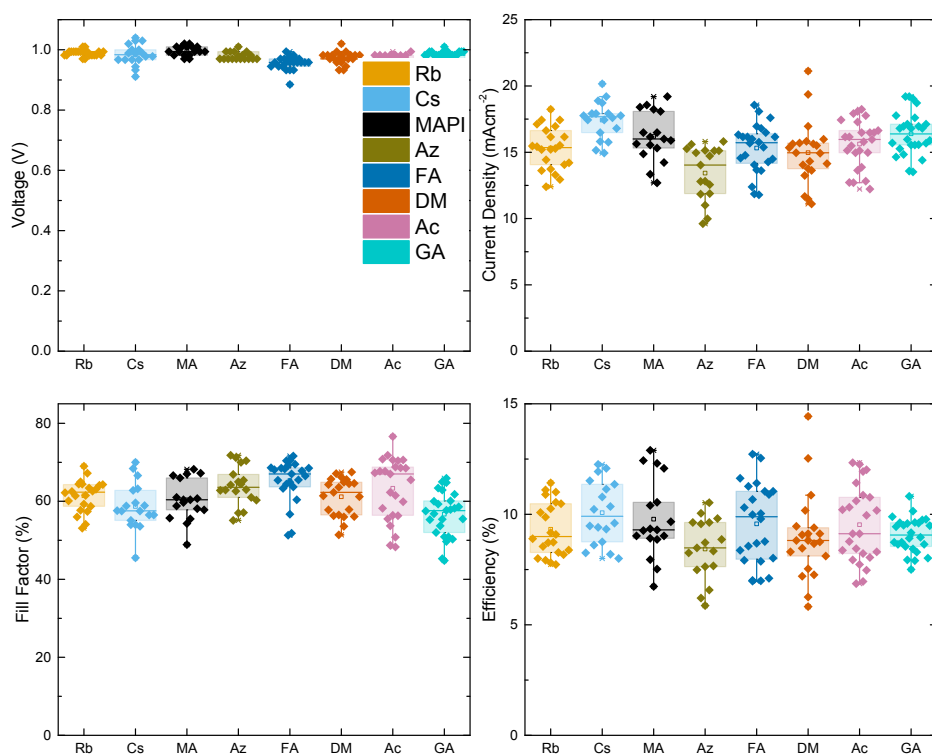


Figure S10. PSC measurements. Box plots for V_{OC}, J_{SC}, Fill factor and efficiency for the cells with different cationic additives.

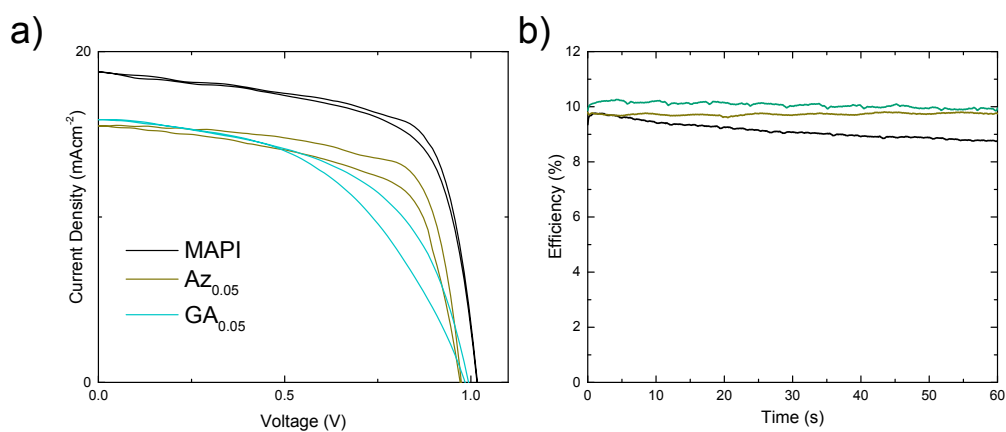


Figure S11. Current-voltage measurements. (a) Representative *JV* curves for MAPbI_3 , $\text{MA}_{0.95}\text{Az}_{0.05}\text{PbI}_3$ and $\text{MA}_{0.95}\text{GA}_{0.05}\text{PbI}_3$ cells and (b) representative stabilised efficiency at the maximum power point for three MA, Az and GA containing cells.

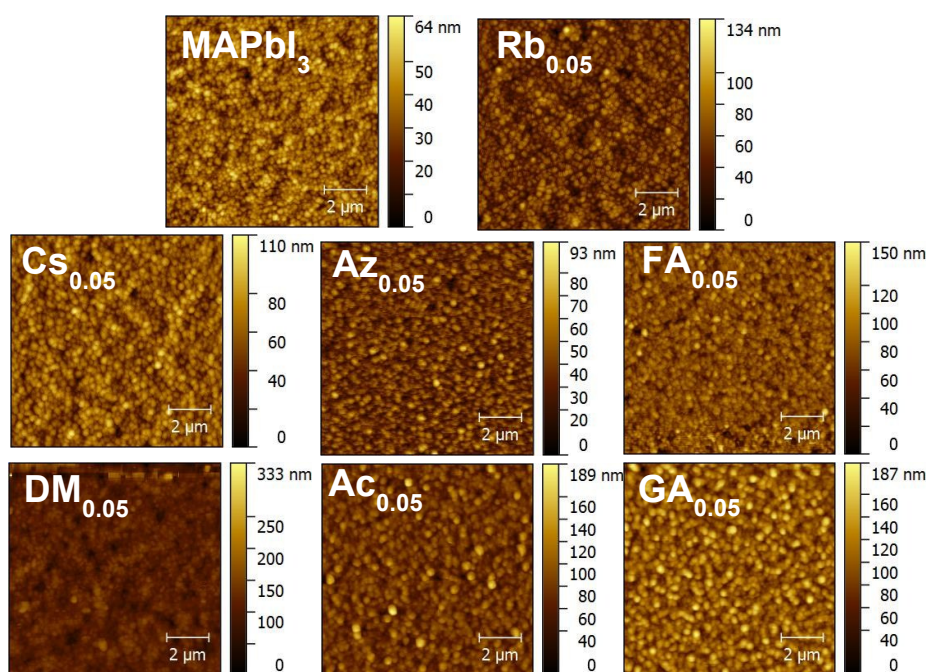


Figure S12. AFM Images for the perovskites with different cation additives.

Table S4. Resistance, Capacitance, mid frequency and low frequency activation energies for mixed-cation films calculated by EIS.

Cation	R_{ct} (Ω)	C_{geo} (nF)	τ (Mid) (s)	E_a (Mid) (eV)	τ (Low) (s)	E_a (Low) (eV)
Rb _{0.05}	55.9	11.9	0.1	N/A	0.77	0.47 (± 0.06)
Cs _{0.05}	35.4	15.4	0.028	0.51	0.63	0.48 (± 0.02)
MA	36.9	13.0	0.00157	0.29	0.02212	0.40 (± 0.08)
Az _{0.05}	49.4	10.3	0.005	0.29	0.5	0.50 (± 0.03)
FA _{0.05}	30.8	15.5	0.01	0.23	0.22	0.54 (± 0.10)
DM _{0.05}	66.0	12.5	0.2	1.16	0.77	0.65 (± 0.08)
Ac _{0.05}	27.3	16.1	0.008	0.31	N/A	N/A
GA _{0.05}	51.9	13.5	0.03	0.38	N/A	N/A

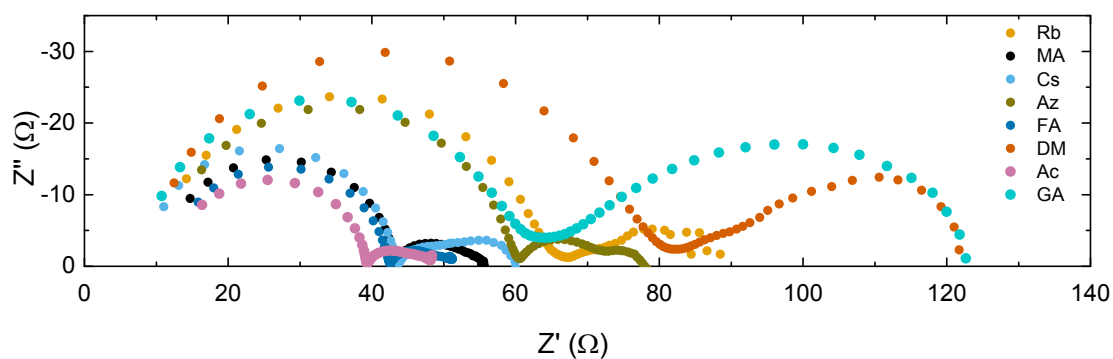


Figure S13. Nyquist plots of all samples at 25 °C.

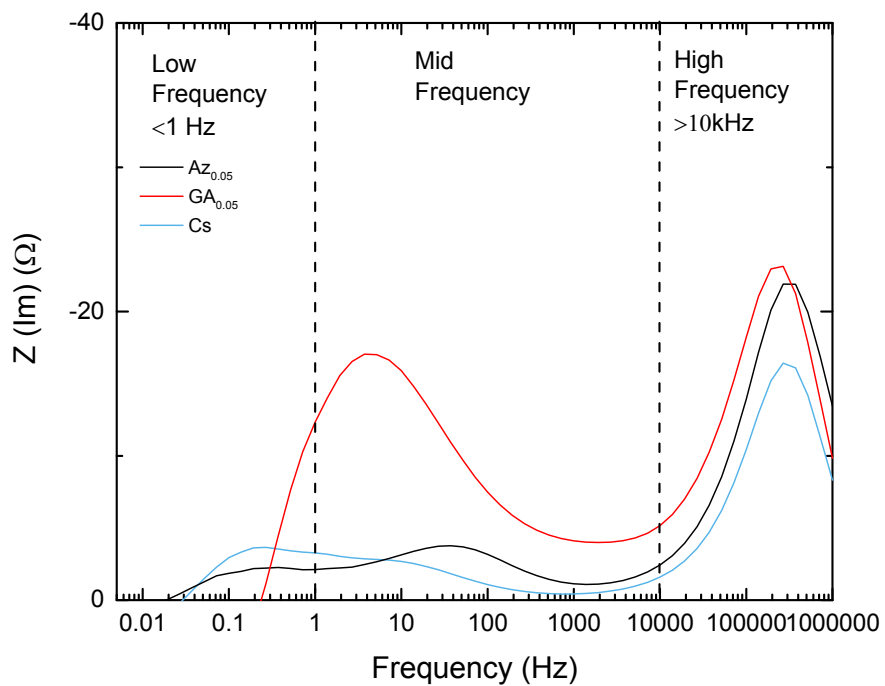


Figure S14. Cole plots for 3 mixed-cation cells.

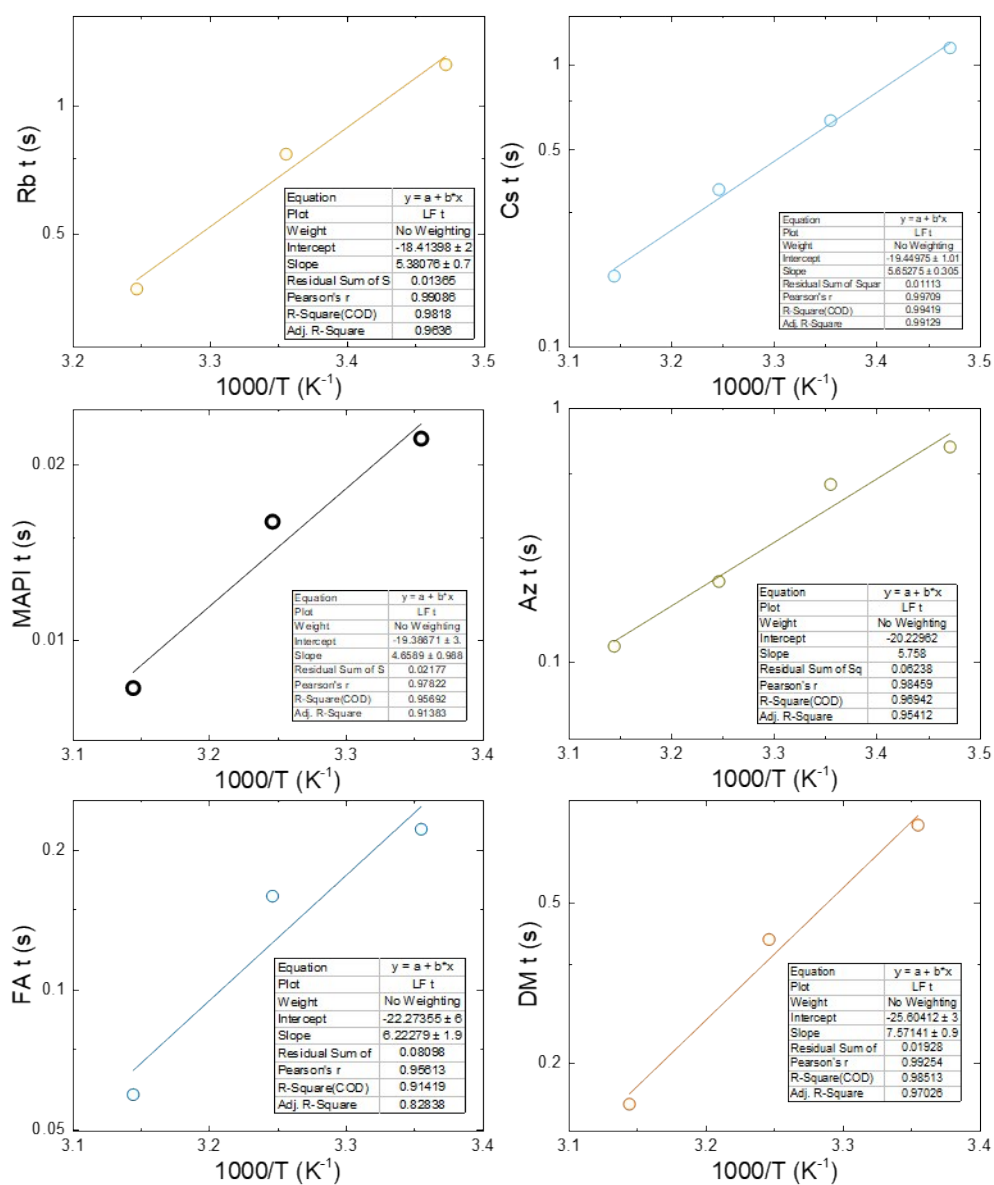


Figure S15. IS measurements. Arrhenius plots for the low-frequency elements of the impedance spectrum, in all samples where it was observed.

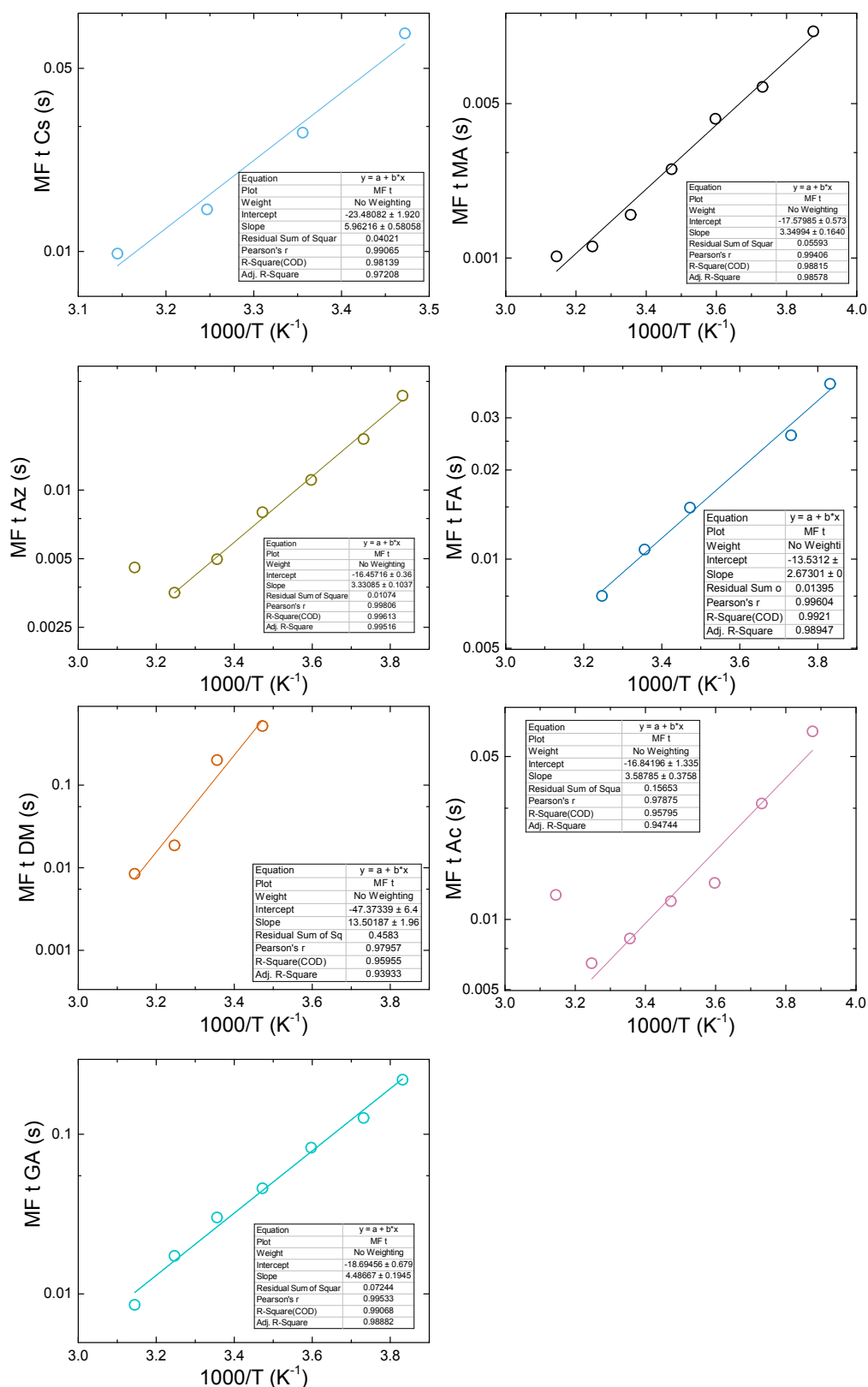


Figure S16. IS measurements. Arrhenius plots for the mid-frequency elements of the impedance spectrum, in all samples where it was observed.

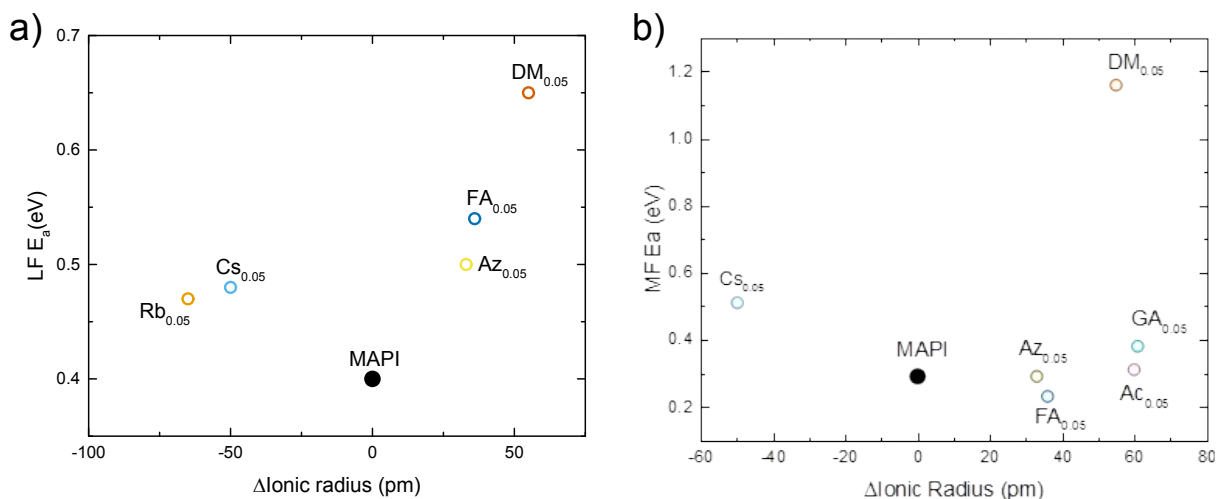


Figure S17. Activation Energies. a) Low Frequency b) Mid Frequency activation energy against the ionic radius relative to MA^+ in $MAPbI_3$. It is important to note that only the low frequency activation energies in (a) are related to iodide motion. The activation energies shown in (b) are obtained from the mid frequency feature and it is not yet known what the physical cause of this feature is. We show the mid frequency activation energies here for completeness.

Figure S17a shows the activation energies of the low frequency feature. Although it has been found that Rb does not act as an A-site cation in FA based perovskites, it can be incorporated alongside other smaller additives.^{11,12} It may act as an A-site cation in the smaller, MA based perovskite. The activation energy of 0.47 eV obtained for $Rb_{0.05}MA_{0.95}PbI_3$ fits the established trend with the other perovskites. The mid-frequency feature for $Rb_{0.05}MA_{0.95}PbI_3$ was not sufficiently resolved and could not be reliably fit.

The MF response is shown in Fig. S16 and S17 (b); and (except for DM) there is a slight decrease in activation energy as larger cations are substituted into the lattice, from 0.58 eV for Am to 0.38 eV for GA. The mid-frequency response in the impedance occurs on the sub-second timescale and is 1-2 orders of magnitude faster than the slow ion reorganisation modulating the response at low frequency. The activation energies are still in the right range for iodide ion conduction and it is possible that fast diffusion of iodide along the surface of crystallites e.g. at the perovskite/HTM or perovskite/ETM interface is modulating the impedance response.

(E) μ SR information

(i) Methods. The positive muons (or anti-muons) used in our experiment are unstable subatomic particles with similar properties to a positron, except their mass is 207 times larger and their lifetime is 2.197 μ s. Muons have been used to study properties such as magnetism and superconductivity in a wide range of different materials.¹³ μ SR has, more recently, been

used to investigate the diffusion of Li^+ and Na^+ in modern battery materials. Muons are implanted into the sample where they decay into a positron, which is most likely to be emitted in the muon spin direction at the instant of decay (Fig. S18). The effect of local fields on the material on the muon spins is detected by the change in the asymmetry of the positron counts in detectors around the sample. Using this technique, activation energies and diffusion coefficients of ions with nuclear magnetic moments can be measured.

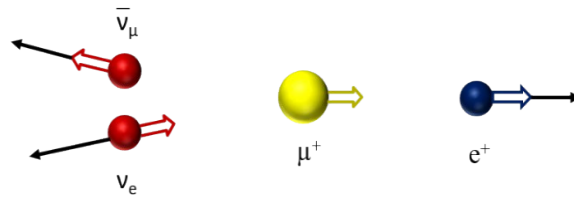


Figure S18. Muon decay. Schematic depicting the decaying of a muon into a positron and two neutrinos.

All the raw muon data is available electronically at the following DOIs, 10.5286/ISIS.E.83552097, 10.5286/ISIS.E.85648377 and 10.5286/ISIS.E.87813248.

The muon data were analysed using the dynamic Gaussian Kubo-Toyabe function multiplied by an exponential to describe the spin evolution of muons within the sample added to a constant background term to account for muons stopping outside the sample. This is shown in the equation below, where A_0 is the initial asymmetry at ($t = 0$), A_{BG} is background asymmetry and A_{KT} is the relaxing asymmetry.¹⁴

$$A_0 P_{LF}(t) = A_{KT} \exp(-\lambda t) G^{DGKT}(\Delta, \nu, t, H_{LF}) + A_{BG}$$

Initial trial fits with all parameters allowed to vary, except for H_{LF} which is controlled by the experimental condition, showed that A_{BG} , A_{KT} and λ were independent of temperature so they were fixed to their mean values in the final analysis. A small non-zero value of λ (*less than 0.02 MHz*) was found to be necessary to consistently describe the data across the full temperature range and can be attributed to a slight difference between the field distribution in the samples and the Gaussian approximation of the G^{DGKT} function.

(ii) Stability of the perovskite powders measured by muon spectroscopy.

Perovskites are known to degrade at higher temperatures, so it was important to check that the material had not been damaged by the measurement. In order to rule out degradation as a cause of the change in the fluctuation data, we investigated the stability of the sample

in three different ways. Firstly, we performed a thermogravimetric analysis on a MAPbI_3 sample between 300 K and 450 K (Fig. S19a, b). No obvious mass loss was observed over this temperature range which is in agreement with previously observed thermal analysis on MAPbI_3 .¹⁵ Secondly, pXRD analysis was performed on the MAPbI_3 sample both before and after the μSR experiments. There were small changes in peak intensity, but an absence of peaks associated with the presence of PbI_2 . This strongly suggests no degradation of the perovskite material had occurred (Fig. S19c). Thirdly, after the initial muon measurements were taken, one of the samples was cooled to 100 K and more data were acquired at a few temperature points. There was no change in the resulting spectra.

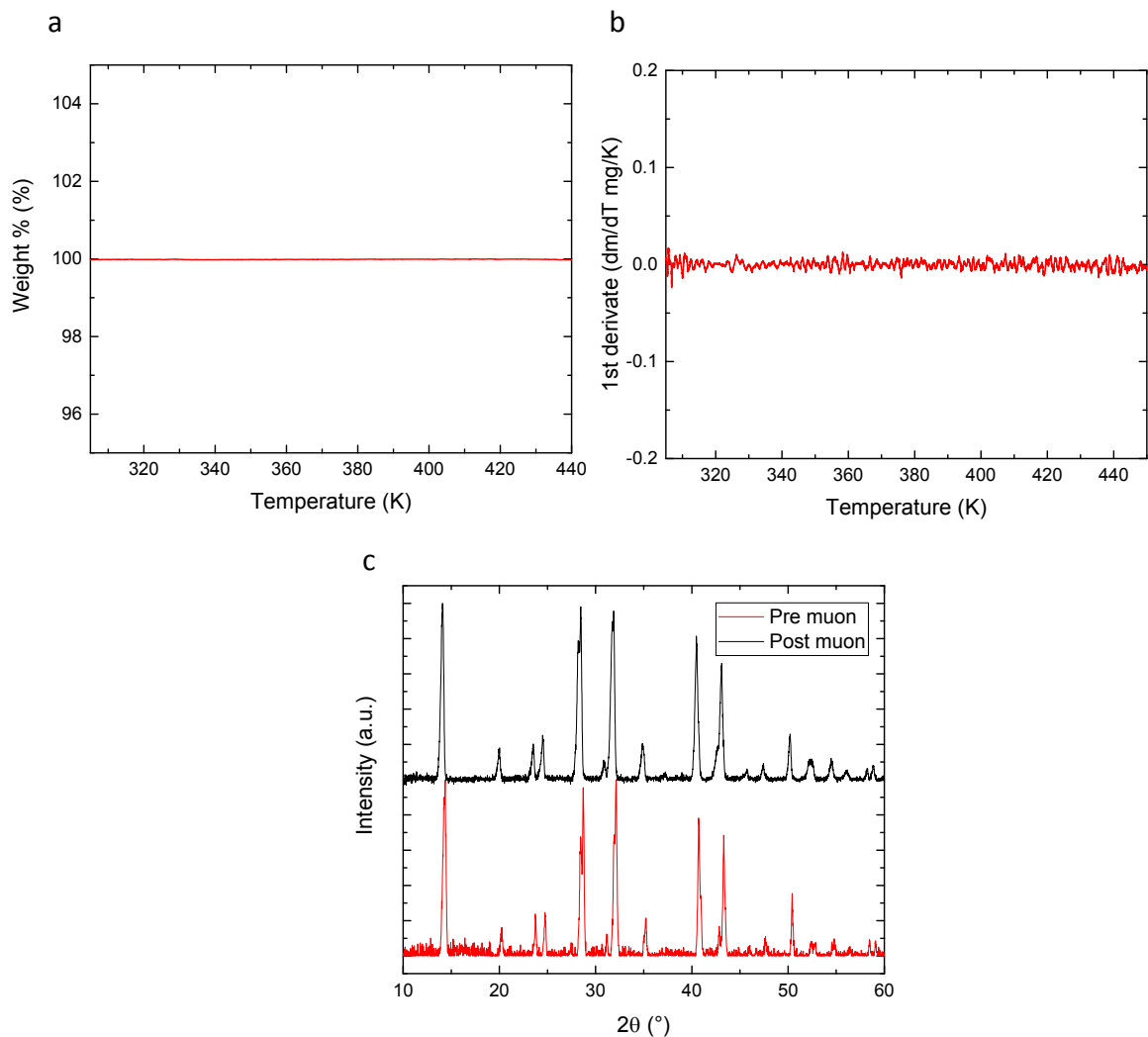


Figure S19. Thermogravimetric analysis. a) Thermogravimetric analysis of MAPbI_3 between 300 K and 450 K. b) The corresponding 1st derivative for MAPbI_3 . c) pXRD of MAPbI_3 before (red) and after (black) the μSR experiment.

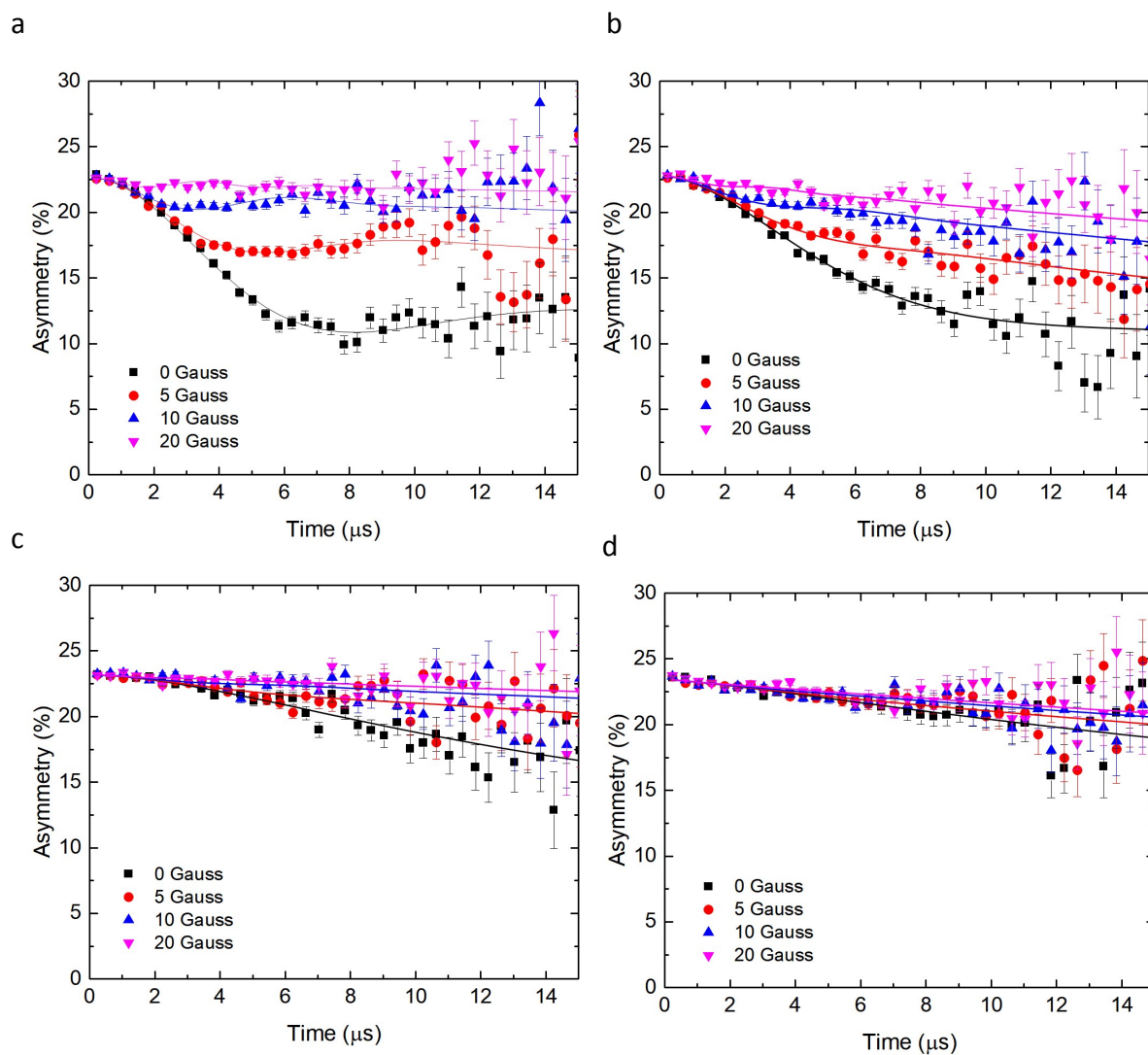


Figure S20. Muon data for MAPbI_3 . Raw muon data for MAPbI_3 at a) 40 K, b) 110 K, c) 350 K and d) 400 K with fits to a dynamic Kubo-Toyabe function with parameters common to the four fields.

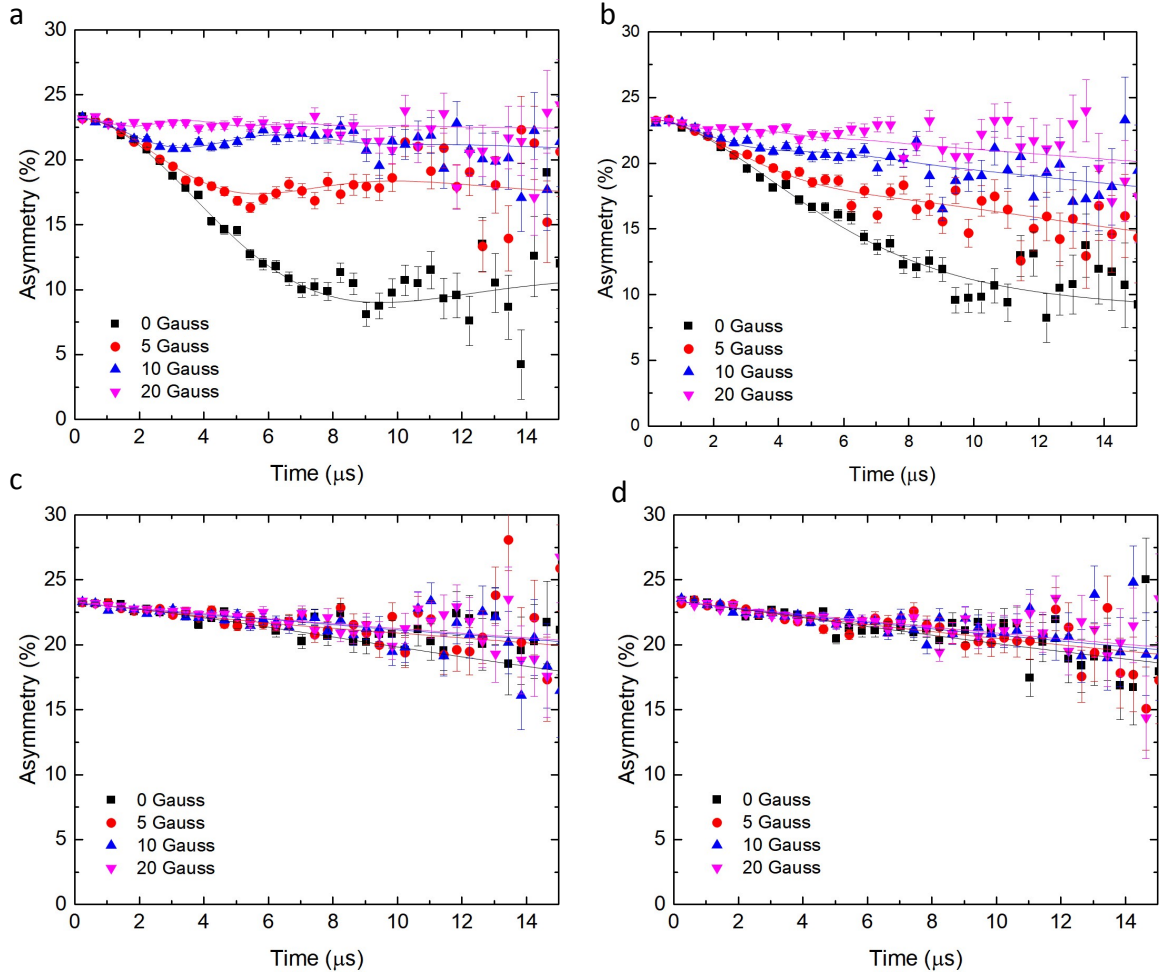


Figure S21. Muon data for d_6 -MAPbI₃. Raw muon data for d_6 -MAPbI₃ at a) 40 K, b) 110 K, c) 350 K and d) 400 K with fits to a dynamic Kubo-Toyabe function with parameters common to the four fields.

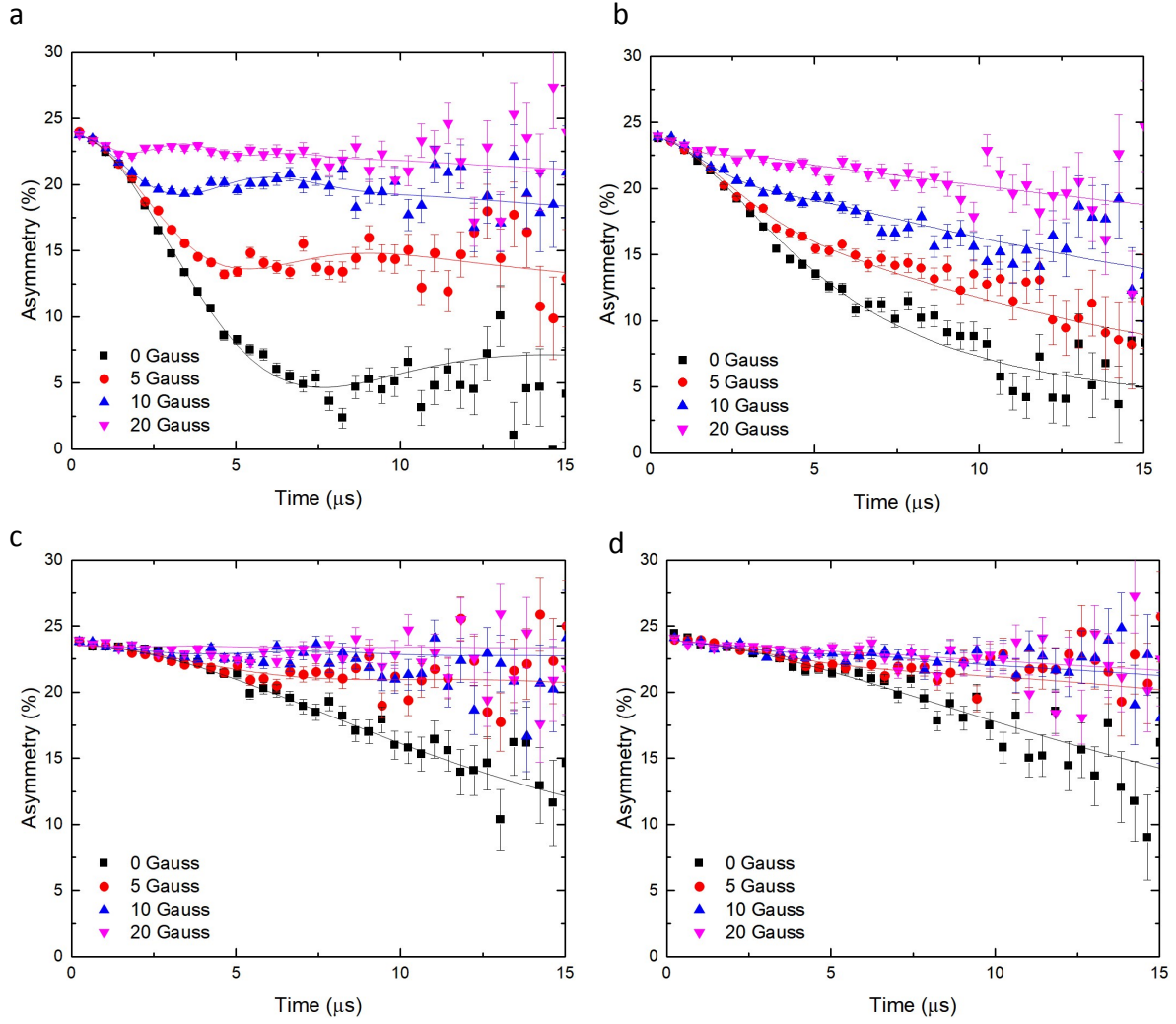


Figure S22. Muon data for $MA_{0.95}GA_{0.05}PbI_3$. Raw muon data for $MA_{0.95}GA_{0.05}PbI_3$ at a) 40 K, b) 110 K, c) 350 K and d) 400 K with fits to a dynamic Kubo-Toyabe function with parameters common to the four fields.

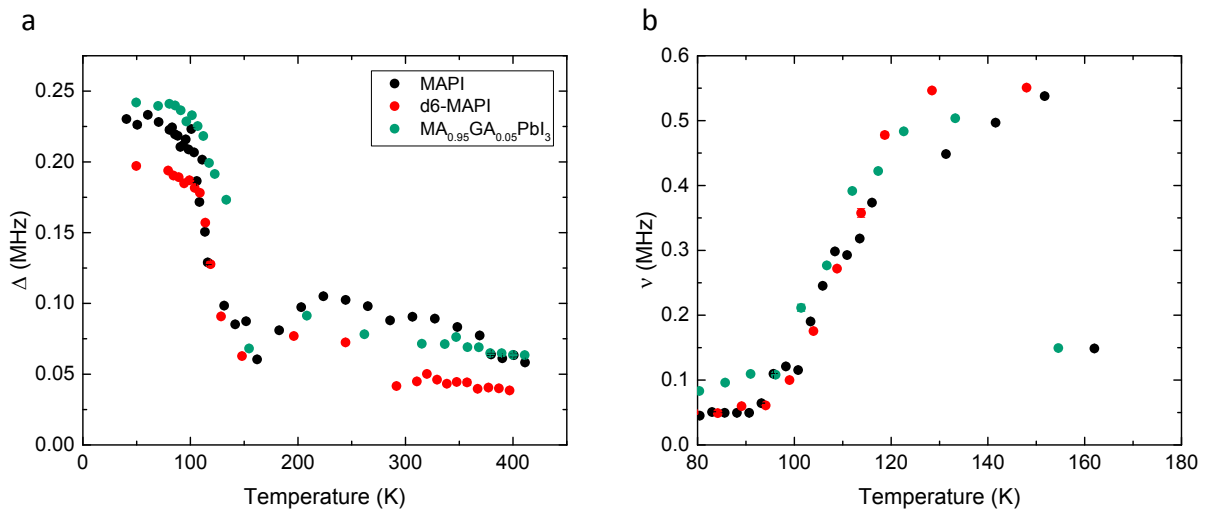


Figure S23. Δ values. a) The temperature dependence of Δ with respect to temperature for MAPbI₃, d₆-MAPbI₃ and GA_{0.05}. b) The temperature dependence of ν for the different perovskites between 80 and 180 K.

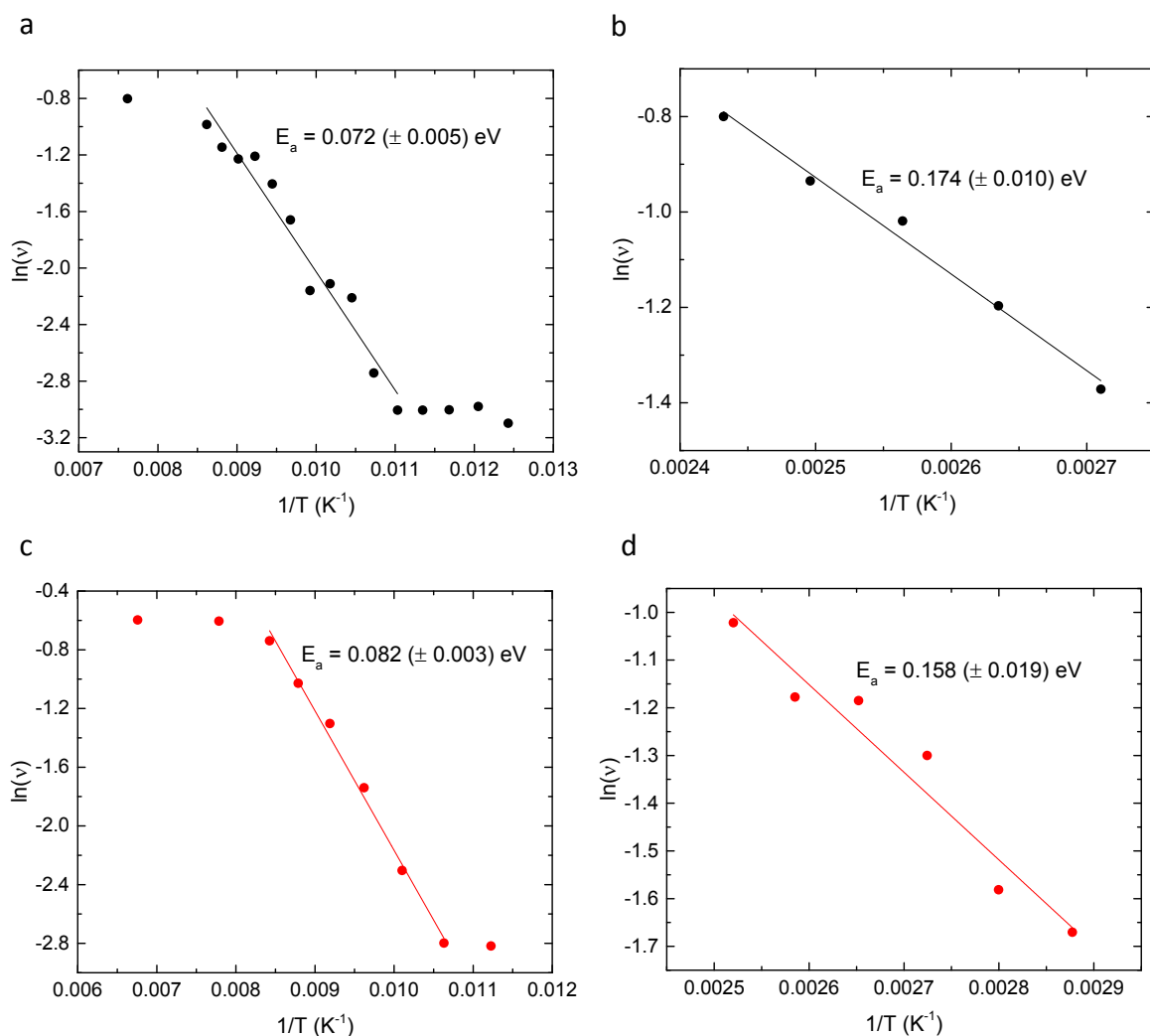


Figure S24. Arrhenius plots of the fluctuation rate for MAPbI₃ (a) 80 K to 115 K, (b) 350 K to 410 K and for d₆-MAPbI₃ (c) 80 K to 115 K and (d) 350 K to 410 K.

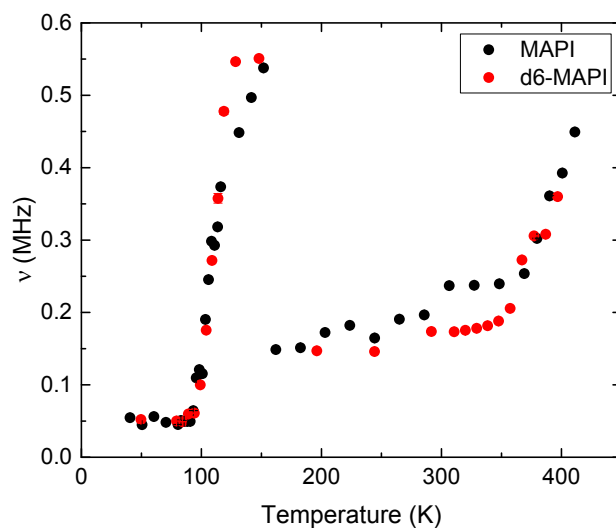


Figure S25. Comparison of ν for MAPI and d_6 -MAPI.

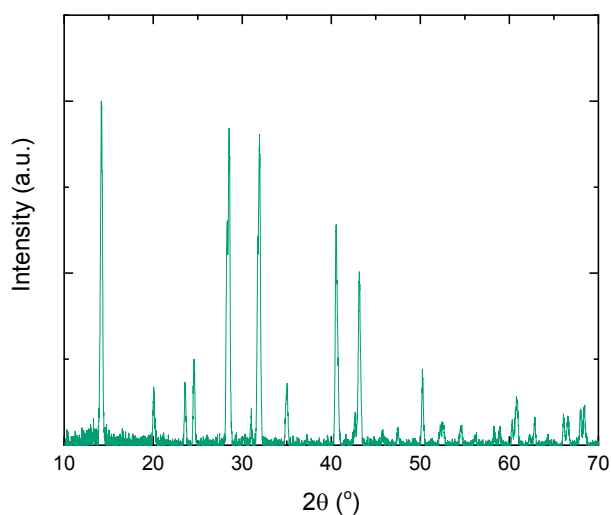


Figure S26. XRD measurements. pXRD analysis of $MA_{0.95}GA_{0.05}PbI_3$

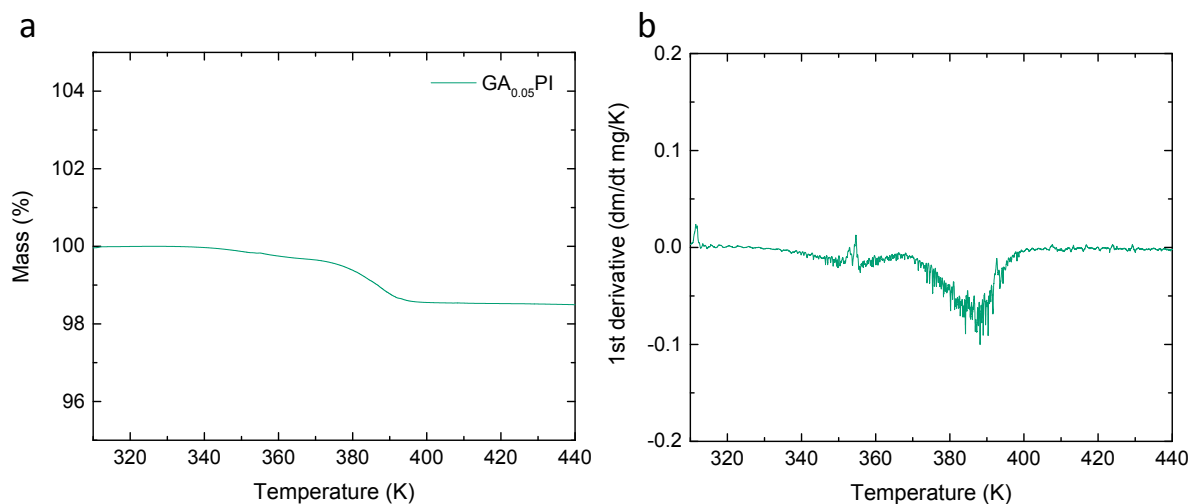


Figure S27. Thermogravimetric analysis. a) Thermogravimetric analysis of $MA_{0.95}GA_{0.05}PbI_3$ between 300 K and 450 K. b) The corresponding 1st derivative.

(iii) Muon Stopping Sites and Local Field Distribution

MAPbI₃ is a very soft and flexible material and behaves quite differently to the more rigid inorganic lattices that are studied for battery materials. It is also important to note that three phase transitions occur during the muon experiments, orthorhombic to tetragonal at about 160 K and tetragonal to cubic at about 330 K.¹⁶

To understand the temperature and phase dependence of the distribution of nuclear magnetic fields, Δ , experienced by the muons; we calculated Δ at different positions in the unit cells of the three structural phases of h6-MAPbI₃ and d6-MAPbI₃. The value of Δ for a given site is defined by the expression:¹⁴

$$\Delta^2 = \frac{2}{3} \mu_0^2 \gamma_\mu^2 \hbar^2 \sum_i \frac{I_i(I_i + 1) \gamma_i^2}{r_i^6}$$

where γ_μ is the gyromagnetic ratio of the muon, I_i and γ_i are the spin and nuclear gyromagnetic ratio of the i -th nucleus, and r_i is the distance between the muon site and the i -th surrounding nucleus. The sum was evaluated for nuclei within a radius of ten-times the longest unit cell parameter, in excess of the distance within which these fields contribute measurably to the observed signal. The positive muons generally stop in the vicinity of negative ions in the crystal. Therefore, the stopping sites of muons in the lattice can be estimated from the electrostatic potential map which has been calculated from *ab initio* computations. As shown in revised manuscript (ESI Fig. S6a-c), the electrostatic potential map of MAPbI₃ suggests that sites near to the iodide ions or to the nitrogen atom (i.e. the negative end of the dipole) of the MA molecule are electronegative and consequently suitable for muon stopping. A further source of information suggesting possible sites is the extensive literature on muons implanted in fluorides. Fluorides give distinct signals due to a coherent bound state of F μ or F μ F that give quantitative information on the bond length(s) involved.^{17,18} Important caveats for such a comparison is that F generally forms ionic bonds whereas I⁻ is generally far more covalent and that no coherent bound states of muons with iodide ions are reported in the literature or evident in our data.

For comparison with the calculations, the typical experimental values of Δ for h₆-MAPbI₃ (d₆-MAPbI₃) in each phase are: orthorhombic 0.22 (0.19) MHz, tetragonal 0.1 (0.08) MHz, and cubic 0.54 (0.37) MHz. Because we are limited to measurements below the decomposition point of MAPbI₃ the values in the cubic phase may not represent the fully developed cubic structure on the MHz timescale. The simplest plausible scenario is the muon forming a bound state of μ I analogous to HI. The bond length of HI is 1.61 Å. If the bond length of μ I scaled in the same way relative to HI as μ F does to HF, this leads to a value of 1.93 Å. These bond lengths suggest 0.07 < Δ < 0.12 MHz due to the iodide ions alone, values comparable

with those observed in the tetragonal and cubic phases but significantly lower than that observed in the orthorhombic phase.

In fluorides, muons more commonly form F- μ -F than F- μ . The valley in the electrostatic potential between neighbouring iodide ions (4.5Å apart) suggests a similar situation is likely here. A linear I- μ -I stopping site appears to give an adequate comparison with the H(D) data for the orthorhombic state $\Delta=0.26$ (0.15)MHz, in the tetragonal state $\Delta=0.11$ (0.07)MHz, and in the cubic phase $\Delta=0.09$ (0.07)MHz. These are in reasonable agreement with the experimental results.

More complex I- μ -I states could also be considered, in analogy with the crooked F- μ -F state associated with PF₆ octahedra discussed in Ref 15. In the orthorhombic phase, neighbouring octahedra tilt in alternating directions so that a triangle of F ions are formed in the (101) plane. . For the centre of this triangle $\Delta=0.227$ (0.220)MHz. This agreement appears very good for H but an overestimate for D. A stopping site intermediate between this and the linear I- μ -I state in the orthorhombic phase, therefore, appears most plausible.

To consider how the 5% cation substitution will affect these stopping sites we carried out electrostatic potential calculations which show very minor changes relative to the unsubstituted material (Fig. S6d,e). The changes in muon stopping site position are therefore likely to be very minor, corresponding to changes in the I- μ -I bond angles due to local lattice distortions rather than different muon stopping sites being favoured. In terms of the Δ values, the principal change will be moving the muon site in the cubic phase closer to coordinating with two iodide ions rather than three, which decreases Δ in agreement with the experimental observations.

If the muon were to implant at the centre of the MA molecule the dipolar field calculations suggest $\Delta\approx 0.65$ MHz and Δ increase towards the end of the electrostatic dipole as the muon gets closer to the protons. Since the observed Δ values are smaller than this, as well as the electrostatic calculations (Fig. S6) suggesting that such a site would be less favourable, we can exclude this site. Similarly, the possibility that muons implant at iodide vacancies is excluded electrostatically.

In conclusion, the temperature dependent behaviour of Δ in h₆-MAPbI₃ and d₆-MAPbI₃ can be explained by muon stopping sites associated with the electrostatically favourable regions between I⁻ ions. The structural changes affect the distances between the MA molecules and the PbI₆ octahedra, in particular, the change in the octahedral tilting. Our data are not consistent with muons stopping in iodide vacancies, or within the MA molecules, or forming μ I bound states. Electrostatic calculations show that the muon stopping sites are strongly

electronegative and this excludes muon diffusion. They also show that the sites will not radically change at a 5% level of cation substitution, even for the GA cation.

(iv) Excluding muon motion in the samples. The growth in ν in the two temperature regions where it is observed could have three plausible origins in these samples: molecular dynamics moving hydrogenated/deuterated ions relative to stationary muons, iodide motion relative to stationary muons, or muon motion relative to the lattice. As discussed in the main text, perdeuteration of the MAPbI₃ sample demonstrated a significant difference in the low-temperature change in ν but not at high temperature, allowing us to attribute the low-temperature behaviour to molecular dynamics of the MA cations.

To distinguish the two remaining possibilities for explaining the high-temperature behaviour we draw an analogy between our muon results and those for the isostructural series LiCrO₂, LiCoO₂, and LiNiO₂.⁴⁴ LiCrO₂ is electrochemically inactive whereas LiCoO₂ and LiNiO₂ both have Li⁺ motion on a timescale amenable to muon study. The high-temperature behaviour observed in our GA sample, where any increase in ν is negligible, is comparable with the results on LiCrO₂. This also agrees with the impedance measurements where the feature related to iodide motion disappears after GA substitution. In contrast, our other samples show significant increases in ν similar to those observed in LiCoO₂ and LiNiO₂. Our samples are also close to isostructural, as the 5% substitution of a second cation slightly distorts the local crystal structure near the substituted cation; but leaves the overall perovskite structure largely unchanged, in good accord with our ab initio simulations and the XRD analysis. Furthermore, we obtain good agreement in the energy scales for iodide motion from the impedance and μ SR measurements, which would be very hard to explain if the latter was observing muon motion rather than iodide motion common to both techniques.

(v) Diffusion coefficient calculations. With the fluctuation data and Equation S1, it is possible to estimate the diffusion coefficient of iodide ions (D_I , Fig. S28.). Where N_i is the number of accessible paths in the i -th path, s_i the jump distance between iodide sites, Z_{vi} the fraction of vacancies present and ν is taken from the muon data.

$$D_I = \sum_{i=1}^N \frac{1}{N_i} Z_{vi} s_i^2 \nu \quad (\text{S1})$$

The iodide diffusion model used for the calculation of diffusion coefficients was that presented by Eames *et al.*¹⁹ This assumes that there is just one mechanism for diffusion with four possible pathways. A jump distance of 4.49 Å, calculated using neutron diffraction data, was used for the inter atomic distance.¹⁰ A vacancy fraction of 0.4%, as calculated by Walsh *et al.*²⁰ was used. We are aware that there is some debate over the precise vacancy fraction in MAPbI₃ and we have used a widely cited literature value. As the diffusion coefficient is linearly dependent on the vacancy fraction, the change can be easily calculated if the vacancy fraction is slightly different.

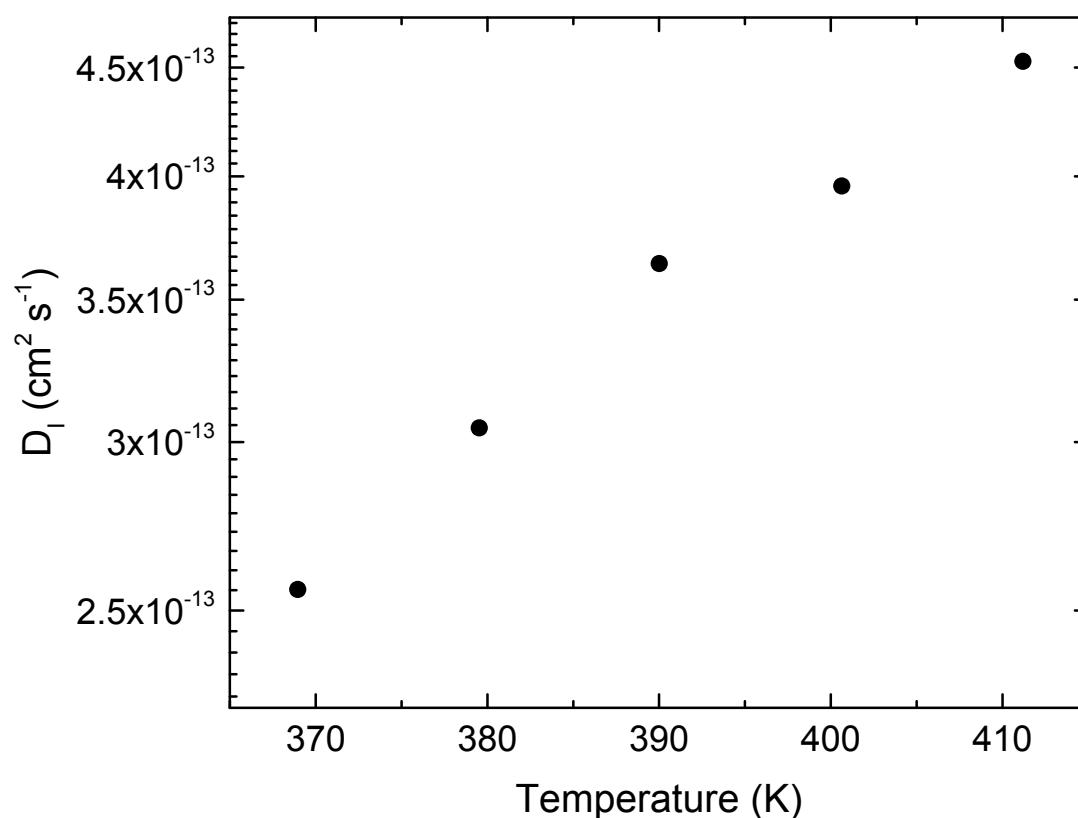


Figure S28. Diffusion coefficients. Calculated diffusion coefficients for iodide in MAPbI₃

References for ESI

1. Pering, S. R. *et al.* Azetidinium lead iodide for perovskite solar cells. *J. Mater. Chem. A* **5**, 20658–20665 (2017).
2. Hutter, J., Iannuzzi, M., Schiffmann, F. & VandeVondele, J. *cp2k*: atomistic simulations of condensed matter systems. *Wiley Interdiscip. Rev. Comput. Mol. Sci.* **4**, 15–25 (2014).
3. VandeVondele, J. *et al.* Quickstep: Fast and accurate density functional calculations using a mixed Gaussian and plane waves approach. *Comput. Phys. Commun.* **167**, 103–128 (2005).
4. Perdew, J. P. *et al.* Generalized gradient approximation for solids and their surfaces. *Phys. Rev. B* **136**, 406, 1–4 (2007).
5. Goedecker, S. & Teter, M. Separable dual-space Gaussian pseudopotentials. *Phys. Rev. B - Condens. Matter Mater. Phys.* **54**, 1703–1710 (1996).
6. Grimme, S., Antony, J., Ehrlich, S. & Krieg, H. A consistent and accurate ab initio parametrization of density functional dispersion correction (DFT-D) for the 94 elements H-Pu. *J. Chem. Phys.* **132**, 154104 (2010).
7. Zhang, Y. Y. *et al.* Intrinsic Instability of the Hybrid Halide Perovskite Semiconductor CH₃NH₃PbI₃*. *Chinese Phys. Lett.* **35**, 036104 (2018).
8. Thind, A. S., Huang, X., Sun, J. & Mishra, R. First-Principles Prediction of a Stable Hexagonal Phase of CH₃NH₃PbI₃. *Chem. Mater.* **29**, 6003–6011 (2017).
9. Frisch, M. J.; Trucks, G. W.; Schlegel, H. B.; Scuseria, G. E.; Robb, M. A.; Cheeseman, J. R.; Scalmani, G.; Barone, V.; Petersson, G. A.; Nakatsuji, H.; Li, X.; Caricato, M.; Marenich, A. V.; Bloino, J.; Janesko, B. G.; Gomperts, R.; Mennucci, B.; Hratch, D. J. Gaussian 16, Revision B.01. (2016).
10. Weller, M. T., Weber, O. J., Henry, P. F., Di Pumpo, A. M. & Hansen, T. C. Complete structure and cation orientation in the perovskite photovoltaic methylammonium lead iodide between 100 and 352 K. *Chem. Commun.* **51**, 4180–4183 (2015).
11. Saliba, M. *et al.* Incorporation of rubidium cations into perovskite solar cells improves photovoltaic performance. *Science (80-.)*. **354**, 206 LP-209 (2016).
12. Zhang, M. *et al.* High-Efficiency Rubidium-Incorporated Perovskite Solar Cells by Gas Quenching. *ACS Energy Lett.* **2**, 438–444 (2017).
13. Cox, S. F. J. Implanted muon studies in condensed matter science. *J. Phys. C Solid State Phys.* **20**, 3187–3319 (1987).
14. Hayano, R. S. *et al.* Zero- and low-field spin relaxation studied by positive muons. *Phys. Rev. B* **20**, 850–859 (1979).
15. Dualeh, A., Gao, P., Seok, S. II & Nazeeruddin, M. K. Thermal Behavior of Methylammonium Lead-Trihalide Perovskite Photovoltaic Light Harvesters. (2014).
16. Whitfield, P. S. *et al.* Structures, Phase Transitions and Tricritical Behavior of the Hybrid Perovskite Methyl Ammonium Lead Iodide. *Sci. Rep.* **6**, 35685 (2016).

17. Brewer, J. H. *et al.* Observation of muon-fluorine ‘hydrogen bonding’ in ionic crystals. *Phys. Rev. B* **33**, 7813–7816 (1986).
18. Lancaster, T. *et al.* Muon-fluorine entangled states in molecular magnets. *Phys. Rev. Lett.* **99**, 1–4 (2007).
19. Eames, C. *et al.* Ionic transport in hybrid lead iodide perovskite solar cells. *Nat. Commun.* **6**, 7497 (2015).
20. Walsh, A., Scanlon, D. O., Chen, S., Gong, X. G. & Wei, S.-H. Self-Regulation Mechanism for Charged Point Defects in Hybrid Halide Perovskites. *Angew. Chemie Int. Ed.* **54**, 1791–1794 (2015).